Journal of Materials Chemistry A

Accepted Manuscript

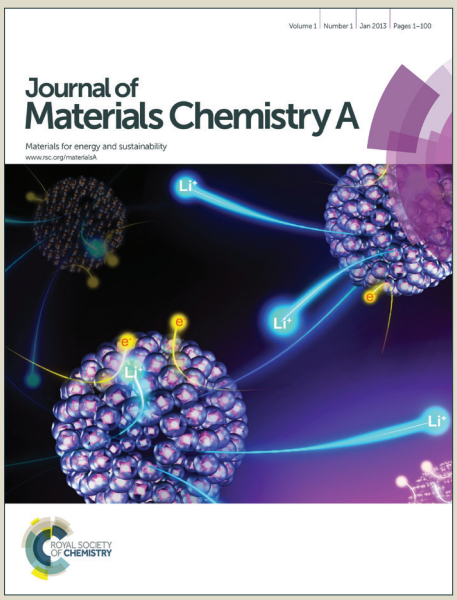

ROYAL SOCIETY OF CHEMISTRY

www.rsc.org/materialsA

Cite this: DOI: 10.1039/c0xx00000x

www.rsc.org/xxxxxx

ARTICLE TYPE

Subunits controlled synthesis of α-Fe_2O_3 multi-shelled core-shell microspheres and effects on lithium/sodium ion batteries performances

Zhen-guo Wu,[a] Yan-jun Zhong,[a] Jie Liu,[b] Jiao-hong Wu,[c] Xiao-dong Guo,[a] Ben-he Zhong,[a] and Zhi-ye Zhang*[a]

Received (in XXX, XXX) Xth XXXXXXXXX 20XX, Accepted Xth XXXXXXXXX 20XX
DOI: 10.1039/b000000x

Two kinds of Fe_2O_3 core-shell microspheres were synthesized. The Fe_2O_3 sample obtained with ethanol (E-Fe_2O_3) contains shell and core assembled by nanoparticles with a diameter of ~150 nm. And the surface is fairly smooth. The Fe_2O_3 with optimized subunits was produced with water (W-Fe_2O_3). The core is assembled by smaller nanoparticles of ~50 nm. The thicker shell and exterior surface possess porous nanorods. These peculiar subunits endow W-Fe_2O_3 with higher specific surface area, more pore volume and larger nanopores. The W-Fe_2O_3 displayed 733.1 mAh g^{-1} at 6000 mA g^{-1}, which is more than two times that of E-Fe_2O_3 (306.5 mAh g^{-1}). Encouragingly, the W-Fe_2O_3 also expressed relatively promising sodium ion battery performances. The significantly different performances between E-Fe_2O_3 and W-Fe_2O_3 can be almost entirely attributed to their distinctive subunits. And the study demonstrated that enhanced lithium/sodium ion storage properties can be achieved by adjusting the subunits.

1. Introduction

Lithium ion battery, which currently dominates the market of portable devices, encounters the challenge of high energy and high energy density for its expanded application in electric vehicles (EVs) and renewable energy storage.[1, 2] And ferric oxides (Fe_2O_3), which possesses advantages of high specific capacity (1007.0 mAh g^{-1}), high safety, non-toxicity, natural abundance and low cost, has been recognised as a potential candidate for commercial anode[3, 4] (graphite: 372.0 mAh g^{-1}). However, the practical application of Fe_2O_3 is still hindered by the electrode pulverization that is caused by large volume changes during charge-discharge processes.[5, 6] Several efforts have been devoted to preparing nanostructured Fe_2O_3 to improve the electrochemical performances, e.g. nanorods,[7, 8] nanotubes,[9] microcubes,[10] and so forth. Among these nanostructures, multi-shelled core-shell Fe_2O_3 microspheres structure with subtle characteristics of internal void and peculiar arrangement of core-shell has attracted special attention.[4, 11-15] Zhu et al. synthesized Fe_2O_3 hollow spheres composed of ultrathin nanosheets by a hard-template method.[16] A capacity of 815.0 mAh g^{-1} could be delivered at 500 mA g^{-1} after 200 cycles. A superior rate capability was also exhibited with 330.0 mAh g^{-1} at 5000 mA g^{-1}. Xu et al. prepared α-Fe_2O_3 multi-shelled hollow spheres using carbonaceous microsphere as templates.[17] The triple-shelled Fe_2O_3 hollow spheres displayed an ultrahigh capacity of 1702.0 mAh g^{-1} after 50 cycles at 50 mA g^{-1} and 1100.0 mAh g^{-1} at 1000 mA g^{-1}. The pioneer studies demonstrate that the yolk-shell structure endows Fe_2O_3 anode with enhanced electrochemical performances. And the results also suggest that subunits of the structure may greatly affect the performances,[18, 19]. However, there are rare reports about the influence of subunits.What's more, from a view of practical application point, the relatively enormous void in the previously reported Fe_2O_3 multi-shelled core-shell hollow spheres causes low volume density, which may severely hamper the enhancement of energy density.[20] And the strategy to recover such key defect deserves great efforts.

The upcoming new market of renewable energy (solar energy, wind power) storage requires large scale production of lithium ion batteries.[21] And the lithium reserves in the earth grow up to be a crucial matter. Uneven distribution of lithium (mostly found in South America) and the extraction processes may bring high cost from a long-term perspective.[22, 23] Among viable scenarios, sodium with the advantages of natural abundance, even distribution, and similarity with lithium is regarded as a candidate to replace lithium.[24, 25] Some previous reports have demonstrated the potential application of Fe_2O_3 in sodium ion battery.[26, 27] Wang and his co-workers obtained hollow Fe_2O_3 nanospheres by a carbon-template method. A capacity of 248 mAh g^{-1} was maintained after 20 cycles at 50 mA g^{-1}.[28] M.valvo obtained nanostructured iron oxide powders with 250 mAh g^{-1} after 60 cycles at 130 mA g^{-1}.[29] Nonetheless, the study of structure designed Fe_2O_3 anode for sodium ion battery is still rarely reported.

In the present study, we focus on the subunits of yolk-shell microspheres. Two kinds of Fe_2O_3 yolk-shell microspheres were synthesized by template-free solvothermal method utilizing water or ethanol as solvent. Both of the two samples possess less internal void. But there are peculiar differences between their subunits. The applications of the as-prepared Fe_2O_3 anodes in lithium/sodium half cell were conducted. The results suggest that the subunits (core, shell and surface) greatly impact the

electrochemical performances. It is also evidenced that Fe_2O_3 yolk-shell microspheres with high volumetric energy density, enhanced cycling performances and excellent rate capability could be obtained by subtle design of subunits.

2. Experimental

2.1 Preparation of α-Fe_2O_3 samples

For the synthesis of W-Fe_2O_3, L-proline (2.0 g) and $Fe(NO_3)_3·9H_2O$ (2.0 g) were dissolved in unionized water (30.0 ml). The resultant mixture was transferred to a Teflon-lined autoclave (50.0 ml) and then maintained at 180°C for 12 h. After reaction, the autoclave cooled to room temperature naturally. The precursor was obtained by centrifuging and sequentially washing with water and ethanol for several times and then dried in a vacuum oven at 80°C for 12 h. Finally, the composite was subjected to annealing at 600 °C for 2 h in air. The W-Fe_2O_3 sample was obtained with simply using ethanol as reaction solvent during the thermal treatment process with other conditions unchanged.

2.2 Characterization and electrochemical measurements

Thermogravimetric analysis was performed on a simultaneous thermal analysis apparatus (SDT Q600, TA instrument). The morphology and structure of the as-prepared sample were characterized by field emission scanning electron microscopy (SEM, HITACHI S-4800), transmission electron microscopy (TEM, JEM 2100), Raman system (Xplora,Horiba) and powder X-ray diffraction (XRD, Philips X'pert Pro Super X-ray diffract meter, Cu Kα radiation) measurements. The specific surface area of the α-Fe_2O_3 sample was determined by Brunauer-Emmett-Teller (BET) method using nitrogen adsorption and desorption isotherms on a Micrometics Tristar 3000 system. X-ray photoelectron spectroscopy (XPS) experiments were carried out on a PHI QUANTUM 2000 instrument.

Electrodes of lithium/sodium half cell were made by spreading a mixture of 75 wt % Fe_2O_3 active material, 15 wt % acetylene black and 10 wt % LA 132 onto copper foil current collectors. The as-prepared electrodes were dried at 80 °C in a vacuum oven for 12 h. Electrochemical properties of the electrodes were monitored by assembling them into coin cells (type CR2025) in an argon-filled glove box with water and oxygen contents less than 0.5 ppm. For lithium half cells, lithium foil served as the counter electrode and polypropylene (PP) film (Celgard 2400) as separator. The electrolyte was made of $LiPF_6$ (1 M) and a mixture of ethylene carbonate (EC)/dimethyl carbonate (DMC)/diethyl carbonate (DEC) in a volume ratio of 1:1:1 with 2wt% vinylene carbonate (VC) as additive (purchased from Tinci Materials Technology Co., Ltd., Guangzhou, China). The sodium half cell was assembled in an analogous way. Metallic Na was used as the counter electrode and glass fiber (GF/A, Whatman) as separator. The electrolyte was made of $NaPF_6$ (1 M) and a mixture of EC/DEC in a volume ratio of 1:1 (purchased from Fosai New Materials Co., Ltd., Jiangsu, China). The cells were galvanostatically charged and discharged on a battery test system (LAND-2001A, Land Electronic Co., Ltd., Wuhan, China) with a cut-off voltage range of 0.01-3.0 V (*vs.* Li/Li^+) and 0.005-3.0 V (*vs.* Na/Na^+). Cyclic Voltammetry (CV) was conducted on a CHI 660D electrochemical workstation (CH Instruments Co., Ltd., Shanghai, China) using coin cell at a scan rate of 0.2 mV s^{-1} with the same cut-off voltage range for galvanostatica test. The

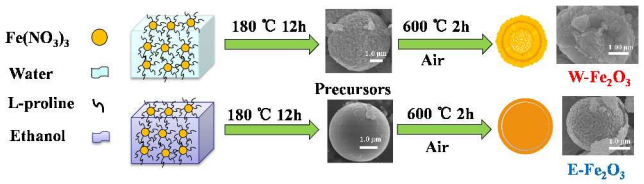

Scheme 1. Schematic flow for synthesis of W-Fe_2O_3 and E-Fe_2O_3.

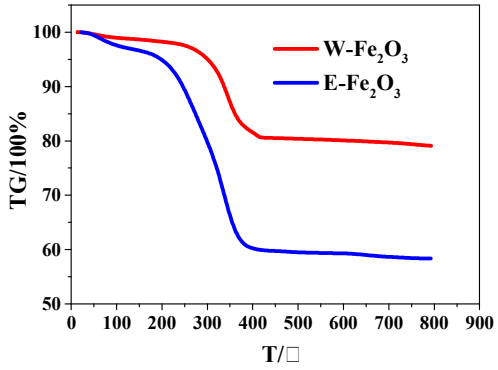

Figure1. TG curves of W-Fe_2O_3 and E-Fe_2O_3 precursors

electrochemical tests were conducted at 30°C.

3. Results and Discussion

Scheme 1 shows the schematic flow for the synthesis of W-Fe_2O_3 and E-Fe_2O_3 via L-proline assisted solvothermal reaction with following annealing in air. Water and ethanol were used to control the subunits. The structural differences between E-Fe_2O_3 and W-Fe_2O_3 maybe related to the different surface tension of ethanol (21.8 mN m^{-1}) and water (72.0 mN m^{-1}).[17] The details of the formation mechanism are an ongoing work and will be discussed in future.

Morphologies of the two precursors have been investigated by SEM and TEM. As shown in Fig S1, some tiny differences between the two precursors could be found. The surface of W-Fe_2O_3 precursor microspheres composed of nanoparticles is quite coarse (Fig S1b, S1c). Conversely, the E-Fe_2O_3 precursor microspheres possess much smooth surface (Fig S1e, S1f). The low magnified images (FigS1a, S1c) indicate that both of the two precursors possess poor conductivity. TEM measurement was used to furtherly identify the structure. Fig S2a indicates that no obvious internal void be detected in W-Fe_2O_3 precursor. And Fig S2b is consistent with the SEM results. However, it could be noticed that the region between edge and core in E-Fe_2O_3 precursor microsphere could be filled by the residue the L-proline (Fig S2c, S2d), which results in final core-shell structure.

TG measurement for the precursors was utilized in determining the calcination process. And the results are shown in Fig 1. The test was conducted from ambient temperature to 800 °C in air with a heating rate of 10 °C min^{-1}. The thermal decompositions of the precursors started from about 300 °C. And the mass of residue stays unchanged at ~500 °C. Therefore, the calcination process was fixed at 600 °C for 2 h to guarantee a complete decomposition of the precursor in a relatively short

time.

The differences in morphology and weight loss of TG curves of the precursors could be related to the different features between water and ethanol containing dielectric constants, dipole moments and surface tension. Water possesses higher dielectric constants and dipole moments, which result in higher polarity. The XRD pattern of W-Fe_2O_3 precursor (Fig S3) indicates that the Fe_2O_3 structure had already been formed after hydrothermal treatment. The $Fe(NO_3)_3{\cdot}9H_2O$ is easily to be ionized in water. The L-proline can also be totally dissolved in water to generate OH^-. The hydrolysis reaction of hydrated iron ions and OH^- will help to form metal hydroxide ($Fe(OH)_3$), which finally result in Fe_2O_3 via dehydration.[20, 30] The large surface tension of water make the diffusion of L-proline and iron ions difficult. Few amphiphilic L-proline molecules may be adsorbed on Fe_2O_3 crystal nucleus. And the weight loss of E-Fe_2O_3 precursor is small. The large surface tension also results in coarse surface as shown in some previous reports.[15, 20] For E-Fe_2O_3 precursor, the low polarity of ethanol results in incompletely dissolution of L-prolineaccordingg to the solubility (1.5 g L-proline/ 100 g ethanol). The small dielectric constant of ethanol make it difficult to perform the hydrolysis and dehydration reactions of iron ions, which is demonstrated by the XRD pattern of E-Fe_2O_3 precursor (Fig S3). The elongation of proline chains by electrostatic cross-linking and the interaction between Fe ions and proline will gather much more proline on the $Fe(OH)_3$ nanocrystal nucleus. The massively undissolved L-proline also can be easily attached to the products of the initial reaction. The low surface tension will facilitate the diffusion of proline and finally result in the relatively smooth surface, which also can be observed previously.[31] The large adsorption capacity of proline in the E-Fe_2O_3 precursor imply a large weight loss in TG curves. Element analysis was carried out to get further information of the precursor. As shown in Table S1, The carbon and nitrogen contents in W-Fe_2O_3 precursor are 10.01wt% and 2.52 wt%. And much higher carbon and nitrogen contents are detected in E-Fe_2O_3 precursor (C: 36.55 wt% ; N: 12.63 wt%). The element analysis results are in consistent with the TG curves and effectively support the above explanation.

After calcination in the air, the composition and structure of the final products were identified by XRD method. The XRD patterns of W-Fe_2O_3 and E-Fe_2O_3 are depicted in Fig 2a. Sharp peaks reveal good crystallinity of the samples. The two samples have peaks at the same position. And the intensity ratios of the peaks are analogous. No impurity phase could be discovered in the XRD patterns. The peaks at

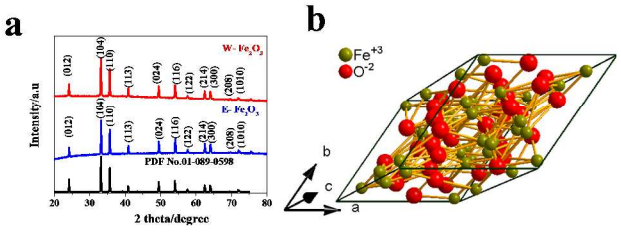

Figure 2. XRD patterns of W-Fe_2O_3 and E-Fe_2O_3 (a); crystal schematic image of Fe_2O_3 with R-3c structure (b).

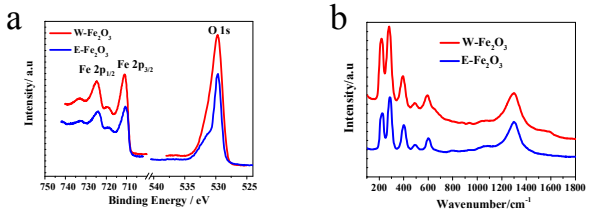

Figure 3. XPS spectra of Fe2p and O1s (a) and Normalized Raman spectra (b) of W-Fe_2O_3 and E-Fe_2O_3.

24.14°, 33.14°, 35.61°, 40.83°, 49.41°, 54.00°, 57.49°, 62.38° ,63.96°, 69.49° and 71.80° can be indexed separately as (012), (104), (110), (113), (024), (116), (122), (214), (300), (208) and (1010) faces of α-Fe_2O_3 (PDF No.01-089-0598) with a space group of R-3c, which is shown in Fig 2b.

XPS and Raman spectra were served to obtain further information of the composition and structure of the samples. XPS determined the chemical state of Fe and O elements in the compounds. Fig 3a shows the high resolution spectra of Fe2p and O1s of W-Fe_2O_3 and E-Fe_2O_3. The two samples display analogous spectral shape and peak position. And the centered binding energies of Fe2p and O1s are located at almost the same positions ($Fe2p_{1/2}$ 724.4 eV, $Fe2p_{3/2}$ 711.0 eV, O1s 529.7 eV), which are in agreement with previous reports of Fe^{3+} and O^{2-}.[32, 33] Raman spectroscopy was carried out with a 532 nm laser as the excitation light. The results (Fig 3b) further demonstrate the structures of Fe_2O_3 samples with a space group of R-3c, which is compatible with the XRD patterns.[34]

Fig 4 displays the SEM and TEM (HRTEM) images of the E-Fe_2O_3. The diameters of the E-Fe_2O_3 microspheres are about 3.0 μm (Fig4a, 4e). The cracked microsphere (Fig 4b) demonstrates the yolk-shell structure. The core and shell are

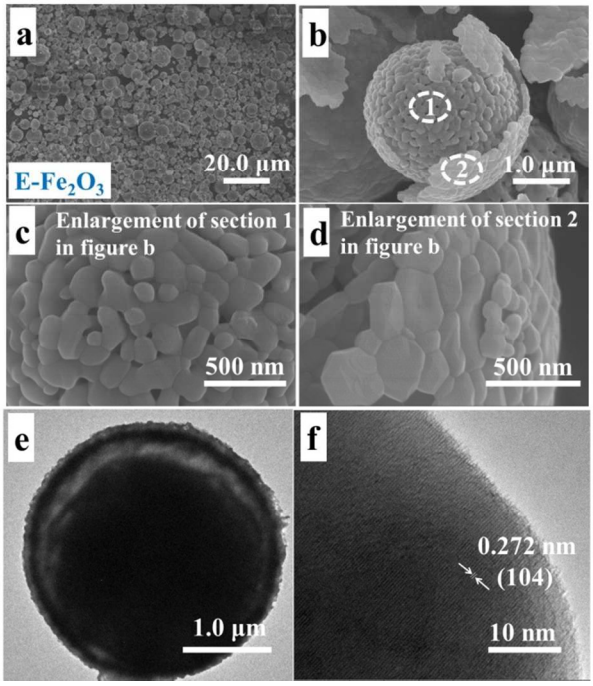

Figure 4. Low-magnification SEM images (a, b), high-magnification SEM images (c, d), TEM image (e), and HRTEM image (f) of E-Fe_2O_3.

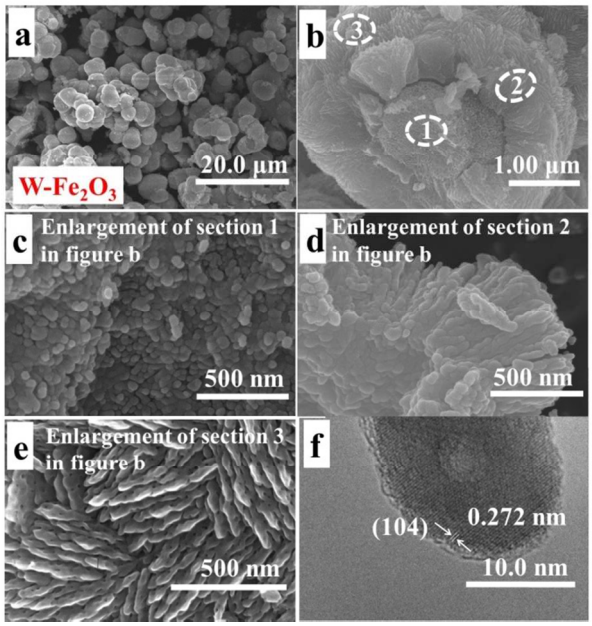

Figure 5. Low-magnification SEM images (a, b), high-magnification SEM images (c, d, e), and HRTEM image of W-Fe_2O_3 (f).

densely assembled by nanoparticles with a diameter of ~150 nm, which are revealed by enlarged images of regional sections (Fig 4c, 4d). TEM result (Fig 4e) is consistent with SEM images, and provides additional evidence of the yolk-shell structure. Minor internal void relatively evenly distributes in the microspheres, and indicates a high volumetric density. Fig 4f is a typical high resolution TEM (HRTEM) image, in which the (104) lattice fringes of α-Fe_2O_3 can be clearly seen. The yolk-shell structure may offer a large contact area between the electrolyte and active materials, facilitating electrochemical reaction. The internal void and hierarchical structure also ensure the structural stability, which contributes to enhanced electrochemical performances.

As shown in Fig 5a and 5b, the W-Fe_2O_3 shows analogous yolk-shell microspheres structure and the similar size to that of E-Fe_2O_3. However, some peculiar subunits with differences would be observed in comparison with E-Fe_2O_3. Firstly, no obviously internal void was observed between the core and shell (Fig 5b), which indicates high volumetric density. Secondly, the core possesses smaller nanoparticles with a diameter of ~50 nm (Fig 5c), which is beneficial for reaction kinetics. Thirdly, thicker shell with a thickness of ~600 nm could better support the structural stability. What's more, the shell is composed of nanorods oriented to the core with a diameter of ~50 nm and a length of ~580 nm (Fig 5d). And the nanoroads facilitate the transportation of electrons and ions. At last, the porous nanorods with a diameter of ~40 nm and a length of ~470 nm (Fig 5e) coated on the exterior of microspheres bring much more rough surface, which would enhance the contact area between active material, carbon black, binder and electrolyte. The (104) lattice fringes of α-Fe_2O_3 also can be noticed from the HRTEM image (Fig 5f). Such artful differences of subunits may greatly affect the physical character (specific surface and so on) and electrochemical performances.

BET measurements were used to estimate the specific area, pore volume and pore size distribution, which are important for anode materials with the large volume change during charge-

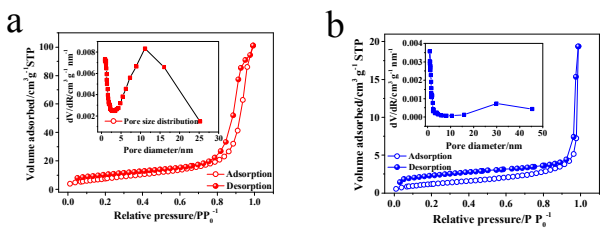

Figure 6. Nitrogen adsorption/desorption isotherms and pore size distribution of the W-Fe_2O_3 (a) and E-Fe_2O_3 (b)

discharge processes. The results reveal that the E-Fe_2O_3 sample has a specific surface area of 5.34 m^2 g^{-1} and a pore volume of 0.030 cm^3 g^{-1} with nanopores. A much higher specific surface area of 35.45 m^2 g^{-1} and a pore volume of 0.145 cm^3 g^{-1} were exhibited by W-Fe_2O_3 due to the different subunits, correspondingly. The N_2 adsorption/desorption isotherms of two samples can be assigned to the type V of the IUPAC classification,[35]which implies the mesoporous structure. In the W-Fe_2O_3 microspheres, there is a mass of nanopores with a diameter ranged from 25 to 5 nm, which could be discovered from the pore size distribution (inset Fig 6a). However, only nanopores below 10nm could be found in the E-Fe_2O_3 sample. It could be declared that the W-Fe_2O_3 possess higher specific area, more pore volume, larger nanopores than that of E-Fe_2O_3, which may provide more lithium/sodium ions storage locations and better reaction kinetics.

The CV curves of W-Fe_2O_3 and E-Fe_2O_3 are shown in Fig 7. The CV curves of W-Fe_2O_3 and E-Fe_2O_3 are analogous, which indicate the similar electrochemical behavior. Two cathodic current peaks at ~0.77 V and ~0.52 V can be clearly observed in the first cycle. The high intense peak initially at 0.52 V shifts to higher potential (0.79 V), and the peak at 0.77 V disappears in the subsequent cycle processes.[15] This can be interpreted by two factors: (1) the lithium insertion into the crystal structure of Fe_2O_3, the reversible conversion reaction of Fe_2O_3 with metallic lithium to form Li_2O and metal (Fe^0), and (2) the inevitable formation of solid electrolyte interphase (SEI) film and irreversible reactions between lithium ions and electrode material. The cathodic peaks shift phenomenon could be related to the electrochemical milling effect of the first cycle, which results in the formation of 1-5 nm metal nanoparticles dispersed into a Li_2O matrix.[36, 37] In the anodic process, a broad peak appears at about 1.69 V, corresponding to the reversible conversion of metallic Fe to iron oxides.[20] In the subsequent cycles, the anodic peak also positive shifts slightly to 1.77 V, which is a common phenomenon for iron oxide anode.[38] And the anodic peaks shift could be related to the unexpected extraction of some Li from Li_2O matrix when oxidizing Fe^0 to Fe^{3+},[39] which has not been clearly identified yet.

The electrochemical process could be summarized as:

$$Fe_2O_3 + 6Li \leftrightarrow 2Fe + 3Li_2O \qquad (1)$$

It should be noticed that the intensity of peaks located at ~0.52 V for W-Fe_2O_3 is relatively stronger than that of E-Fe_2O_3, which may be due to the more lithium ion storage locations and better reaction kinetics induced by peculiar subunits.

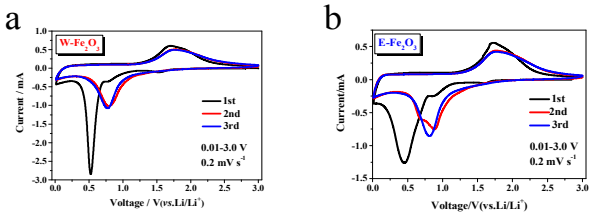

Figure 7. The CV curves of W-Fe_2O_3 (a) and E-Fe_2O_3 (b).

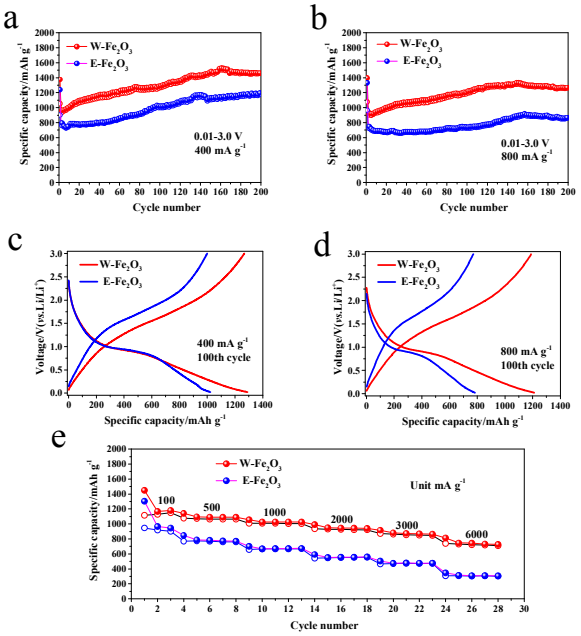

Figure 8. Cycling performances of W-Fe_2O_3 and E-Fe_2O_3 samples at different current densities: 400 mA g^{-1} (a), 800 mA g^{-1} (b); Charge-discharge curves of 100th cycle at 400 mA g^{-1}(c) and 800 mA g^{-1} (d); rate capability (e).

Fig 8 presents the electrochemical performances of W-Fe_2O_3 and E-Fe_2O_3 samples. Both of the two samples showed enhanced cycling performances. The capacities tend to be stable after several cycles. And relatively high capacities of the two anodes can be retained after a long-term cycling. No fast capacity fade phenomenon was observed, which indicates good structural stability of W-Fe_2O_3 and E-Fe_2O_3 anodes. As shown in Fig 8a, W-Fe_2O_3 displayed 1440.9 mAh g^{-1} at 400 mA g^{-1} after 200 cycles, which is ~22.7% higher than that of E-Fe_2O_3 with 1174.6 mAh g^{-1}. When the current density increased to 800 mA g^{-1}, W-Fe_2O_3 still delivered excellent capacity of 1264 mAh g^{-1} after 200 cycles (Fig 8b) with an increment rate of ~46.5% than that of E-Fe_2O_3 (862.6 mAh g^{-1}). Even more strikingly, the W-Fe_2O_3 possess better rate capability with 750.4 mAh g^{-1} at 6000 mA g^{-1}(Fig 8e), which is more than two times that of E-Fe_2O_3(315.8 mAh g^{-1}). It's worth mentioning that the enhanced performances of the two samples presented here are comparable or superior to that of some remarkable previous research on Fe_2O_3 yolk-shell microspheres.[12, 13, 16, 17, 33]

The capacity fluctuation phenomenon during cycling test (Fig 8a, 8b) could be partly ascribed to the reversible growth of a polymeric gel-like film on the surface of the progressively pulverized particles resulting from electrochemical grinding effect, which is agreement with previous reports of transition metal oxides. [16, 20] The charge-discharge curves of 100th cycle (Fig 8c, 8d) demonstrated the consistent electrochemical behavior with CV profiles. It also can be observed that the W-Fe_2O_3 sample exhibit reduced polarization and better reaction kinetics compared with E-Fe_2O_3, which also can be observed from CV results.

The morphology of the electrodes after 200 cycles at 400 mA g^{-1} was presented to illustrate the structural stability. As shown in Fig 9, the structures of W-Fe_2O_3 and E-Fe_2O_3 microspheres can be well preserved after long time cycling. Some tiny morphology changes of subunits could be found with a careful observation. The nanoparticles and porous nanorods of the W-Fe_2O_3 had become larger than the original state (Fig 9c, 9d).

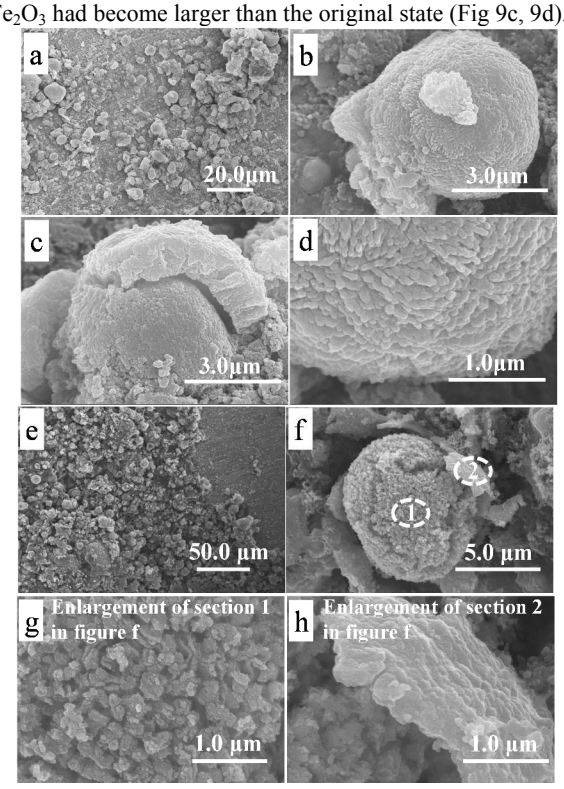

Figure 9. SEM images of W-Fe_2O_3(a,b,c,d) and E-Fe_2O_3 (e,f,g,h) after 200 cycles at 400 mA g^{-1}

The trace of the collapse of nanoparticles in the E-Fe_2O_3 can be clearly seen from Fig 9g and 9h. These morphology changes reveal that the volumetric strain can be relieved by variations of subunits without obvious overall structure collapse.

The applications in sodium ion battery of Fe_2O_3 anodes were also conducted. Fig 10a shows the CV curves of W-Fe_2O_3 in the sodium half cell. The analogous reaction with lithium half cell is expected to take place, which should yield a capacity of 1007 mAh g^{-1} and a volume change of about 215%. However, sodium ions possess larger size, higher atomic mass and reduced mobility than that of lithium ions. And these features make sodium ions more difficult than lithium ions to complete the reaction. The result indicates that the conversion process upon sodiation/desodiation of Fe_2O_3 is not similar to the lithiation/delithiation reaction. Some differences also can be found in the solid electrolyte interphase (SEI) forming stage. Two reductive peaks around 0.76 and 0.02 V (*vs*. Na/Na^+) are observed at the first cycle. And the peak around 0.02 V

disappears during subsequent cycles. This phenomenon could be attributed to the following processes: (1) the sodium ions insertion into the crystal structure of Fe_2O_3, which forms Na_xFeO_2 compound, the reversible reduction reaction of Fe_2O_3 to form metal (Fe^0); and (2) the inevitable formation of SEI film and some side reactions between electrolyte and electrode materials.[1, 26, 29] Two broad oxidative peaks around 1.0 and 1.5 V can be ascribed to the oxidation of Fe^0 to Fe_2O_3. An increase of the anodic current around 2.9 V is also previously reported without clear explanation yet.[29] The electrochemical behavior of E-Fe_2O_3 is analogous to that of W-Fe_2O_3 (Fig 10b). The reductive peak around 0.50 V indicates larger polarization of E-Fe_2O_3 in comparison with the W-Fe_2O_3. The representative charge-discharge curves at 40 mA g^{-1} of W-Fe_2O_3 and E-Fe_2O_3 samples are depicted in Fig 10c, 10d. The voltage plateaus observed

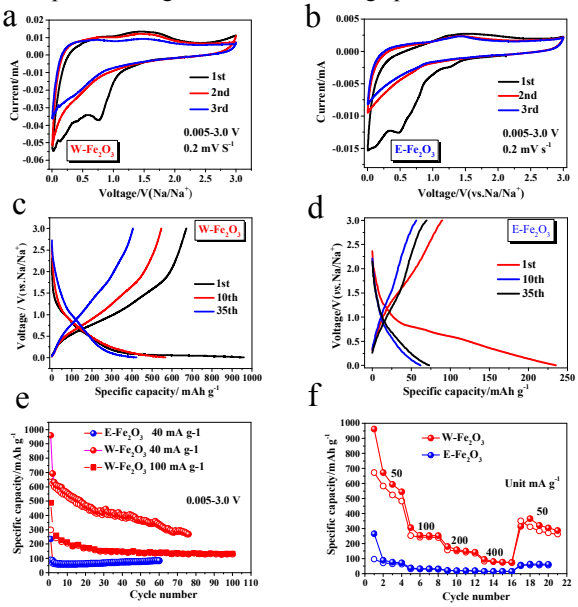

Figure 10. (a,b) CV plots for the W-Fe_2O_3 and E-Fe_2O_3 electrodes in a Na half cell;(c,d) selected charge-discharge curves of W-Fe_2O_3 and E-Fe_2O_3 at 40 mA g-1; (e) cycling performances of W-Fe_2O_3 and E-Fe_2O_3 at 40 mA g-1;(f) rate capability of W-Fe_2O_3 and E-Fe_2O_3.

from the curves are consistent with that of CV profiles. And a larger polarization can be obviously observed for E-Fe_2O_3 (Fig 10d). Fig 10e gives the cycling performance comparison of the two samples. It's clear that W-Fe_2O_3 expressed superior performances to E-Fe_2O_3 in sodium half cell, which is consistent with the results in lithium ion battery. For W-Fe_2O_3, a reversible charge capacity of 671.9 mAh g^{-1} was obtained in the first cycle at 40 mA g^{-1}. And 288.0 mAh g^{-1} could be maintained after 70 cycles, which demonstrate a relative outperformed cycling stability. When the W-Fe_2O_3 anode was tested at 100 mA g^{-1}, 129.0 mAh g^{-1} could be retained after 100 cycles. However, only 81.9 mAh g^{-1} could be delivered after 60 cycles at 40 mA g^{-1} for E-Fe_2O_3. The rate performances illustrated in Fig 10f were conducted at 50, 100, 200 and 400 mA g^{-1}. The corresponding capacities are 595.1, 249.2, 151.1 and 75.0 mAh g^{-1}, respectively. When the current varies back to 50 mA g^{-1}, a high capacity can still be recovered. In contrast, the rate capability of E-Fe_2O_3 anode with only 15.0 mAh g^{-1} is delivered at 400 mA $g^{-1}$is much worse than that of W-Fe_2O_3. The poor rate performances of sodium ion cells in comparison with that of lithium ion cells could be attributed to the intrinsic feature of sodium, including larger radius, high mass and less movability.[25] Nonetheless, the performances of W-Fe_2O_3 presented here are competitive with some previous results.[26, 28, 29]

The investigation of the electrodes in sodium half cells after cycling was also conducted by SEM. Surprisingly, there are obvious differences about structural revolutions between the two samples. As displayed in Fig11, the morphology of W-Fe_2O_3 change a lot after 70 cycles at 40 mA g^{-1}. The outline of the microspheres was kept with a hollow structure (Fig 11b). It could be noticed that the shell and surface could be preserved (Fig 11c, 11d). The core was almost completely cracked (Fig 11b), which was caused by large strain during sodiation and desodiation processes. Conversely, only some superficial changes of E-Fe_2O_3 could be inspected on the surface (Fig11g, 11h). Considering the awful electrochemical performances, the results suggest that the E-Fe_2O_3 anode show much less reaction activity in sodium half cell, which maybe related to the large primary particle.[28, 29]

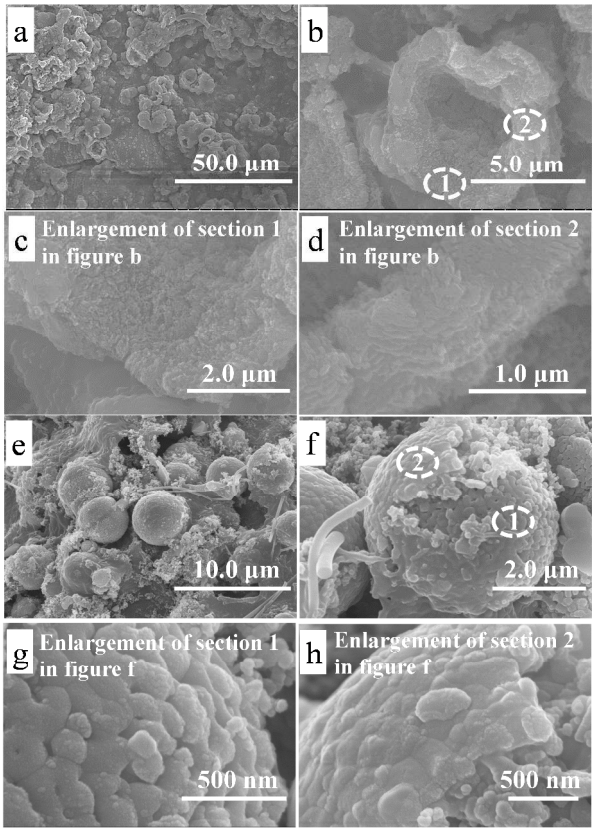

Figure 11. SEM images of W-Fe_2O_3 sample after 70 cycles at 40 mA g^{-1} (a~d) and E-Fe_2O_3 sample after 60 cycles at 40 mA g^{-1} (e~h) in sodium half cell.

Finally, we try to make an analysis of the relation between subunits and ultimate electrochemical performances. The structural schemes of the W-Fe_2O_3 and E-Fe_2O_3 microspheres are revealed in Fig 12. The core-shell structure of E-Fe_2O_3 anode with evidently internal void could enlarge the electrolyte-electrode contact area, facilitate the permeation of electrolyte and accommodate the volume change associated with charge-discharge processes. Such features finally result in excellent cycling performance and rate capability of the lithium ion battery.

Though there is no distinct void between core and shell in W-Fe_2O_3 microspheres, the higher specific surface area, more pore volume and larger nanopores revealed by BET measurement indicate that the W-Fe_2O_3 also possesses enough internal void existed in small units.And these peculiar features can also provide large electrolyte-electrode contact area, advance the infiltration of electrolyte and help to relief the volume change strain.

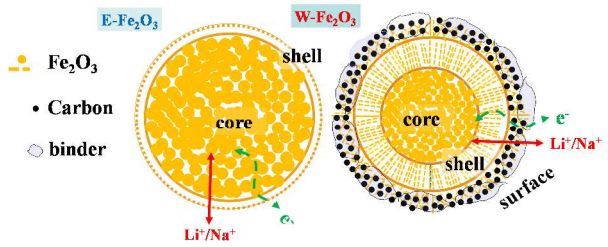

Figure 12. Schematic structural illustration of the W-Fe_2O_3 and E-Fe_2O_3.

At the same time, the higher specific surface area, more pore volume and nanopores can offer more locations for Li ions storage.[40] The nanopores can serve as nanoreactors to afford ideal reaction surroundings for electrode and electrolyte. What's more, the core possesses smaller nanoparticles and the thick shell assembled by 1 D structured nanorods facilitate the electron and Li ions diffusion, which are beneficial for rate capability and buffer the volume change. Finally, the coarse surface coated by nanorods can enhance the contact area between active material, carbon black, binder and electrolyte. And the coarse surface would furtherly result in better electrode conductivity, stronger cohesive force on the current collector and better reaction kinetics. Such artful subunits finally result in superior electrochemical performances in comparison with the E-Fe_2O_3 in lithium ion battery. Inspiringly, the W-Fe_2O_3 also expressed attractive sodium ion storage performances, though the intrinsic feature of sodium, including larger radius, high mass and less movability may impede the charge-discharge processes.

4. Conclusions

In summary, two kinds of Fe_2O_3 multi-shelled core-shell microspheres with less internal void were synthesized by a template-free solvothermal method. The differences of subunits were controlled separately by using ethanol (E-Fe_2O_3) or water (W-Fe_2O_3) as solvent. The study demonstrates that the subunits greatly affect the final electrochemical properties. The W-Fe_2O_3 with peculiar subunits displayed more superior performances to E-Fe_2O_3, with 1264.0 mAh g^{-1} retained after 200 cycles at 800 mA g^{-1} and 733.1 mAh g^{-1} at 6000 mA g^{-1} in lithium ion battery. Though the W-Fe_2O_3 have shown potential application in sodium ion battery properties, much more study is required to furtherly enhance the electrochemical performances. At last, the study evidenced that Fe_2O_3 multi-shelled core-shell microspheres anode integrating high volumetric energy density, excellent cycling performance and remarkable rate capability could be obtained by simply optimizing the subunits. And it's believed that the current study can provide an effective strategy to design better electrode materials for lithium/sodium ion battery.

Notes and references

[a] *School of Chemical Engineering, Sichuan University, Chengdu,610065 (PR China); E-mail:nic1201@163.com*
[b] *College of Chemistry and Chemical Engineering, Xiamen University, Xiamen,361005 (PR China)*
[c] *School of Energy Research, Xiamen University, Xiamen,361005 (PR China)*

Acknowledgements
This work was supported by the Science and Technology Pillar Program of Sichuan Province (2014GZ0077), the Youth Foundation of Sichuan University (No. 2011SCU11081), the Doctoral Program of Higher Education of China (No. 20120181120103), and the Open Found of National Engineering Center for Phosphorus Chemical Industry (2013LF1012).

1. Y. Jiang, M. Hu, D. Zhang, T. Yuan, W. Sun, B. Xu and M. Yan, *Nano Energy*, 2014, 5, 60-66.
2. P. Poizot, S. Laruelle, S. Grugeon, L. Dupont and J. M. Tarascon, *Nature*, 2000, 407, 496-499.
3. Y. Jiang, D. Zhang, Y. Li, T. Yuan, N. Bahlawane, C. Liang, W. Sun, Y. Lu and M. Yan, *Nano Energy*, 2014, 4, 23-30.
4. X. Li, L. Qiao, D. Li, X. Wang, W. Xie and D. He, *J. Mater. Chem.A*, 2013, 1, 6400-6406.
5. M. Chen, J. Liu, D. Chao, J. Wang, J. Yin, J. Lin, H. Jin Fan and Z. Xiang Shen, *Nano Energy*, 2014, 9, 364-372.
6. H. Dong, Y. Xu, M. Ji, H. Zhang, Z. Zhao and C. Zhao, *Electrochim. Acta*, 2015, 151, 118-125.
7. G. Gao, L. Yu, H. B. Wu and X. W. David Lou, *Small*, 2014, 10, 1741-1745.
8. L. Chen, H. Xu, L. e. Li, F. Wu, J. Yang and Y. Qian, *J. Power Sources*, 2014, 245, 429-435.
9. Z. Wang, D. Luan, S. Madhavi, C. Ming Li and X. Wen Lou, *Chem. Commun.*, 2011, 47, 8061-8063.
10. L. Zhang, H. B. Wu, S. Madhavi, H. H. Hng and X. W. Lou, *J. Am. Chem. Soc.*, 2012, 134, 17388-17391.
11. B. Wang, J. S. Chen, H. B. Wu, Z. Wang and X. W. Lou, *J. Am. Chem. Soc.*, 2011, 133, 17146-17148.
12. L. Zhou, H. Xu, H. Zhang, J. Yang, S. B. Hartono, K. Qian, J. Zou and C. Yu, *Chem Commun (Camb)*, 2013, 49, 8695-8697.
13. M. Y. Son, Y. J. Hong, J.-K. Lee and Y. Chan Kang, *Nanoscale*, 2013, 5, 11592-11597.
14. Y. Li and J. Shi, *Advanced Materials*, 2014, 26, 3176-3205.
15. Z.-g. Wu, Y.-j. Zhong, J.-T. Li, X.-d. Guo, L. Huang, B.-h. Zhong and S.-G. Sun, *J. Mater. Chem.A*, 2014, 2, 12361-12367.
16. J. Zhu, Z. Yin, D. Yang, T. Sun, H. Yu, H. E. Hoster, H. H. Hng, H. Zhang and Q. Yan, *Energ. Environ. Sci*, 2013, 6, 987-993.
17. S. Xu, C. M. Hessel, H. Ren, R. Yu, Q. Jin, M. Yang, H. Zhao and D. Wang, *Energ. Environ. Sci*, 2014, 7, 632.
18. K.-A. Kwon, H.-S. Lim, Y.-K. Sun and K.-D. Suh, *J. Phys. Chem. C*, 2014, 118, 2897-2907.
19. H. Liu and G. Wang, *J. Mater. Chem.A*, 2014, 2, 9955-9959.
20. J. Zhang, Y. Sun, Y. Yao, T. Huang and A. Yu, *J. Power Sources*, 2013, 222, 59-65.
21. B. Koo, S. Chattopadhyay, T. Shibata, V. B. Prakapenka, C. S. Johnson, T. Rajh and E. V. Shevchenko, *Chem. Mater.*, 2013, 25, 245-252.
22. B. Philippe, M. Valvo, F. Lindgren, H. Rensmo and K. Edström, *Chem. Mater.*, 2014, 26, 5028-5041.
23. S. Y. Hong, Y. Kim, Y. Park, A. Choi, N.-S. Choi and K. T. Lee, *Energ. Environ. Sci*, 2013, 6, 2067.
24. H. Li, C. Wu, F. Wu and Y. Bai, *Acta Chim. Sinica*, 2014, 72, 21-29.
25. N. Yabuuchi, K. Kubota, M. Dahbi and S. Komaba, *Chem. Rev.*, 2014, 114, 11636-11682.

26. Z. Jian, B. Zhao, P. Liu, F. Li, M. Zheng, M. Chen, Y. Shi and H. Zhou, *Chem. Commun.*, 2014, 50, 1215-1217.
27. M. C. López, P. Lavela, G. F. Ortiz and J. L. Tirado, *Electrochem. Commun.*, 2013, 27, 152-155.
28. S. Wang, W. Wang, P. Zhan and S. Jiao, *ChemElectroChem*, 2014, 1, 1636-1639.
29. M. Valvo, F. Lindgren, U. Lafont, F. Björefors and K. Edström, *J. Power Sources*, 2014, 245, 967-978.
30. H. Hayashi and Y. Hakuta, *Materials*, 2010, 3, 3794-3817.
31. H.-J. Kim, K.-I. Choi, A. Pan, I.-D. Kim, H.-R. Kim, K.-M. Kim, C. W. Na, G. Cao and J.-H. Lee, *J. Mater. Chem.*, 2011, 21, 6549.
32. H. Xia, W. Xiong, C. K. Lim, Q. Yao, Y. Wang and J. Xie, *Nano,Res.*, 2014, 7, 1797-1808.
33. Q. Wu, G. Wu, L. Wang, W. Hu and H. Wu, *Mater. Sci. Semicond. Process.*, 2015, 30, 476-481.
34. M. V. Reddy, T. Yu, C. H. Sow, Z. X. Shen, C. T. Lim, G. V. Subba Rao and B. V. R. Chowdari, *Adv. Funct. Mater.*, 2007, 17, 2792-2799.
35. M. Kruk and M. Jaroniec, *Chem. Mater.*, 2001, 13, 3169-3183.
36. F. Cheng, K. Huang, S. Liu, J. Liu and R. Deng, *Electrochim. Acta*, 2011, 56, 5593-5598.
37. P. Poizot, S. Laruelle, S. Grugeon, L. Dupont and J. M. Tarascon, *J. Power Sources*, 2001, 97-98, 235-239.
38. Y. Xu, G. Jian, Y. Liu, Y. Zhu, M. R. Zachariah and C. Wang, *Nano Energy*, 2014, 3, 26-35.
39. G. F. Ortiz, I. Hanzu, P. Lavela, J. L. Tirado, P. Knauth and T. Djenizian, *J. Mater. Chem.*, 2010, 20, 4041.
40. J. Liu, H. Xia, D. Xue and L. Lu, *J. Am. Chem. Soc.*, 2009, 131, 12086-12087.

Graphic Abstract

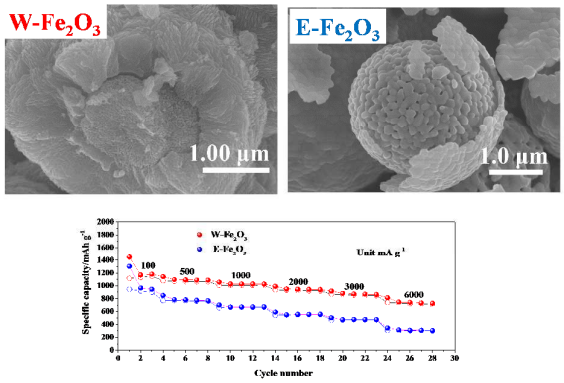

Two kinds of Fe_2O_3 yolk-shell microspheres with different subunits were synthesized by solvothermal method. The subunits were optimized by controlling the solvent. The applications of Fe_2O_3 anodes in lithium and sodium ion battery demonstrate that the distinctive subunits greatly affect the ultimate electrochemical performances.